Materials analysis using fast ions

A. Denker, W. Bohne, J. Rauschenberg, J. Röhrich and E. Strub
Ionenstrahllabor, Hahn-Meitner-Institut, Berlin, Germany

Abstract
Materials analysis with ion beams exploits the interaction of ions with the electrons and nuclei in the sample. Among the vast variety of possible analytical techniques available with ion beams we will restrain to ion beam analysis with ion beams in the energy range from one to several MeV per mass unit. It is possible to use either the back-scattered projectiles (RBS – Rutherford Back Scattering) or the recoiled atoms itself (ERDA – Elastic Recoil Detection Analysis) from the elastic scattering processes. These techniques allow the simultaneous and absolute determination of stoichiometry and depth profiles of the detected elements. The interaction of the ions with the electrons in the sample produces holes in the inner electronic shells of the sample atoms, which recombine and emit X-rays characteristic for the element in question. Particle Induced X-ray Emission (PIXE) has shown to be a fast technique for the analysis of elements with an atomic number above 11.

1 Introduction

When energetic ions impinge material, different interactions between the ion and the atoms in the sample may occur and, in principle, all of them may be employed for the analysis of the irradiated material. For instance, light emitted under ion irradiation is used for the so-called ionoluminescence, providing information about the chemical state of the elements in the sample. The current induced by ions in electronic devices may be utilized to measure the electronic properties of a device (ion beam induced current – IBIC). Among the vast variety of possible analytical techniques, we confine to those using ion beams in the energy range of a few MeV per mass unit and where the interaction between ion and atom in the sample can be considered to be a binary process, involving the projectile ion and a single target atom:

- elastic atomic collisions: They happen at very low energies, typically below a few keV and are, therefore, not included in this paper. They are used for Ion Scattering Spectrometry (ISS), providing information about the surface composition and structure.

- inelastic atomic collisions: When a fast moving charged particle collides with an atom, an electron may ejected from an inner atomic shell leading to the emission of X-rays, characteristic for the emitting atom. This technique, the Particle Induced X-ray Emission, allows the detection of elements with an atomic number above 11.

- elastic nuclear collisions of the projectile with the atomic nucleus in the target: Either the backscattered ions are detected (Rutherford-Back Scattering – RBS) or the recoiled atoms of the sample are measured (Elastic Recoil Detection Analysis – ERDA).

- inelastic nuclear collisions: They occur at higher energies as the projectiles have to overcome the Coulomb barrier of the target nuclei and are the base of Nuclear Reaction Analysis (NRA).

After a short discussion of the energy loss effects, we will describe the various analytical techniques in more detail. Textbooks [1–3] are recommended for more detailed information.

2 Energy loss

A detailed description for all processes relevant to the energy loss of ions in matter is beyond the scope of this paper. In this sections, just the necessary basis for ion beam analysis are mentioned.

All the interactions between the projectile ion and the target atoms result in slowing down the ion. This energy loss depends on the ion species, charge state, ion energy, and target material. The specific energy loss, or stopping power *S*, is defined as:

$$\lim_{\Delta x \to 0} \frac{\Delta E}{\Delta x} = \frac{dE}{dx}(E) \tag{1}$$

At low ion energies, when the velocity of the ion is significantly lower than the Bohr velocity, the stopping power is dominated by elastic collisions with the target nuclei. Hence, this is called the nuclear stopping region. With increasing ion energy, the nuclear stopping decreases with 1/E. For higher energies, the electronic energy loss, i.e. the interaction of ions with the target electrons, becomes the dominant process. Therefore, two regions can be distinguished: The Lindhard regime, where the stopping power scales with $E^{1/2}$ and the Bethe-Bloch region where the stopping power scales with E^{-1}(see Fig. 1).

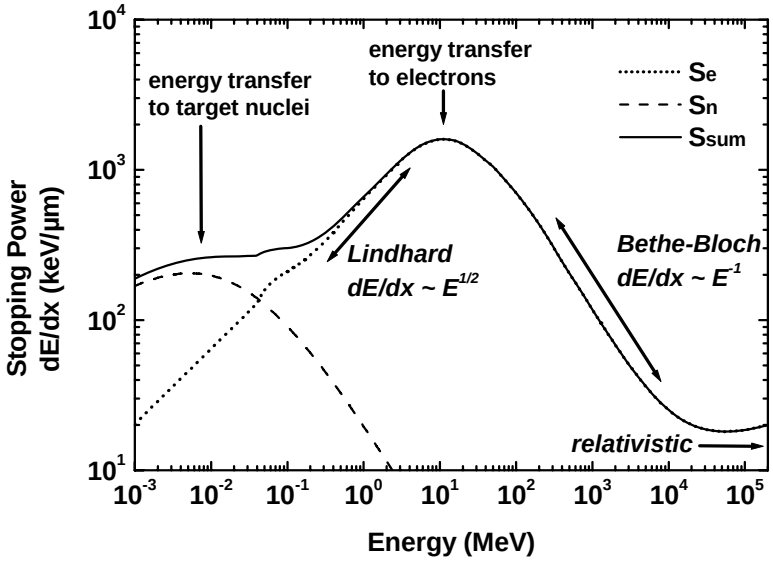

Fig. 1: Stopping power of ^{20}Ne in polyethylene, calculated with SRIM 2003. The dotted line gives the nuclear stopping, the dashed line the electronic stopping and the solid line the sum.

Besides a huge amount of experimental data and fits to them [4,5], in ion beam analysis quite often the program SRIM [6] is used for the calculation of the stopping powers. SRIM provides also data for the projected ranges of the ions and their lateral straggling (see Table 1).

Table 1: Calculated energy loss, ranges and lateral straggling of ions in silicon

Ion and energy	S_n (keV/µm)	S_e (keV/µm)	Range (µm)	Lateral straggling (µm)
p, 3 MeV	0.01	20	92	4.1
p, 68 MeV	0.001	1.8	21 000	860
He, 3 MeV	0.17	190	12	0.49
^{197}Au, 350 MeV	90	19 000	30	0.91

3 PIXE – Particle Induced X-ray Emission

3.1 Basics of PIXE

Emission of X-rays by charged particles was observed first by Chadwick [7] using alpha particles from a radioactive source. In 1913 Moseley found empirically the following correlation between the frequency ν of the K_α line and Z:

$$\sqrt{\nu K_\alpha} = k(Z-1) \tag{2}$$

with $k^2 = 2.48 \cdot 10^{15}$ Hz. The determination of the X-ray energy allows the identification of the emitting element.

The arrival of the lithium drifted Si(Li) detectors in the late 60s lead to the energy-dispersive spectroscopy of X-rays, allowing the simultaneous detection of X-rays originating from various elements. One can consider the publication of Johansson et al. in 1970 [8] as starting of PIXE. They used proton beams of 2 to 3 MeV energy from a Van de Graaff accelerator and targets consisting of carbon foils with subnanogram depositions of Ti and Cu. Since that time, PIXE has evolved tremendously, being applied in archaeometry, biology, geosciences, medicine, and environmental studies. Under favorable conditions, detection limits below 1 ppm can be achieved.

For the excitation of characteristic X-rays also electron beams, X-rays from X-ray tubes or radioactive sources may be applied. The X-ray excitation cross sections of MeV ions and of electrons with an energy of 10 to 50 keV, as used in electron microprobes, are similar. However, the Bremsstrahlung background for electrons is much higher due to the fast deceleration of electrons in the sample. Therefore the detection limits in PIXE are generally two orders of magnitude lower. In addition, the range of electrons in the sample is in the order of 1 µm, whereas the range of a 1 MeV proton beam is at least 5 times larger as can be seen in Fig. 2. The excitation with X-ray tubes or radioactive sources leads also to higher background in the spectra, due to photon scattering on the sample. In addition, the intensity of particles from a radioactive source are several orders of magnitude smaller than from an accelerator, and the accelerator has the additional advantage of the possibility to focus the beam down to sub-millimeter diameter. Although all ions can be used for the excitation of characteristic X-rays, light ions provide less background to the spectrum, so that today the acronym PIXE is also interpreted as Proton Induced X-ray Emission.

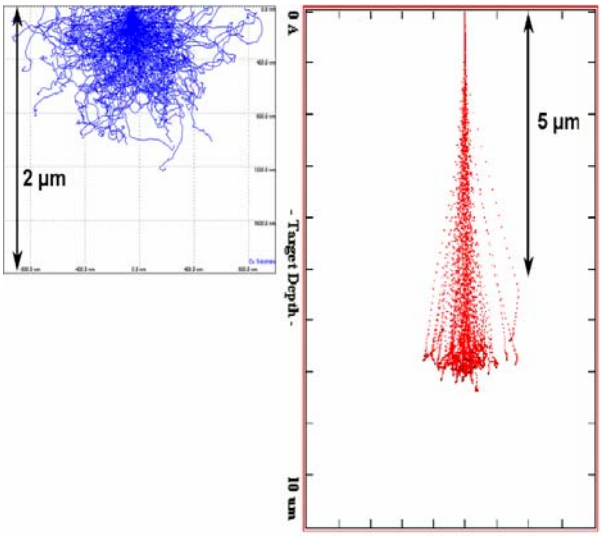

Fig. 2: Calculated paths of 20 keV electrons (SREM [9,10]) and 1 MeV protons (SRIM [6]). The range for protons is much larger and the lateral straggling is smaller.

As already mentioned above, the basic process of PIXE is the inelastic scattering of the projectile with the target atom, leading to excitation of the atom and subsequent ionization if the kinetic energy of the projectile is larger than the binding energy of the electron. This is always the case for PIXE, where the ion energy is usually in the MeV range. To fulfill the principle of momentum, the nucleus of the atom takes a part of the momentum. Hence, the probability of ionization is greatest for the inner electron shells (K, L) due to the strong coupling to the nucleus. The ionized atom de-excite within 10^{-16} s either by the emission of a characteristic X-ray or an Auger electron. The probability of the emission of a characteristic X-ray, the so-called fluorescence yield increases with Z as shown in Fig. 3. The fluorescence yield is quite well known and can be calculated using the formula of Bambynek et al. [11,12]. The low probability of characteristic X-ray emission for light elements is one reason that light elements are not detectable by PIXE.

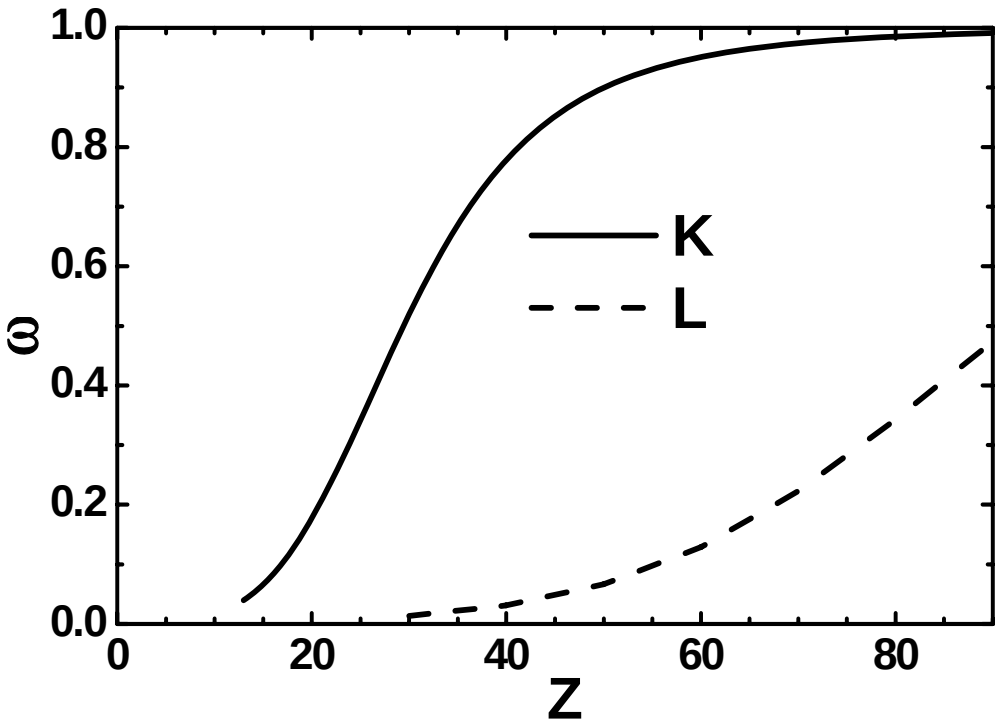

Fig. 3: The X-ray fluorescence yield ω of K and L shell as a function of Z

The orbital angular momentum *l* and the spin *s* of the electrons interact, leading to the fine structure of the electron shells (see Fig. 4). The total angular momentum *j* is given by:

$$\vec{j} = \vec{l} + \vec{s} \tag{3}$$

Electrons filling a vacancy in the K or L shell have to fulfill the rules $\Delta l = \pm 1$, and $\Delta j = 0, \pm 1$. For K lines, the relative intensity of the various lines is known with an accuracy of a few percent [13]. For the L lines the situation is more complicated, as before de-excitation by a L X-ray or an Auger electron the vacancy may be filled with an electron of the same shell at a higher energy. This transition is known as the Coster-Kronig effect.

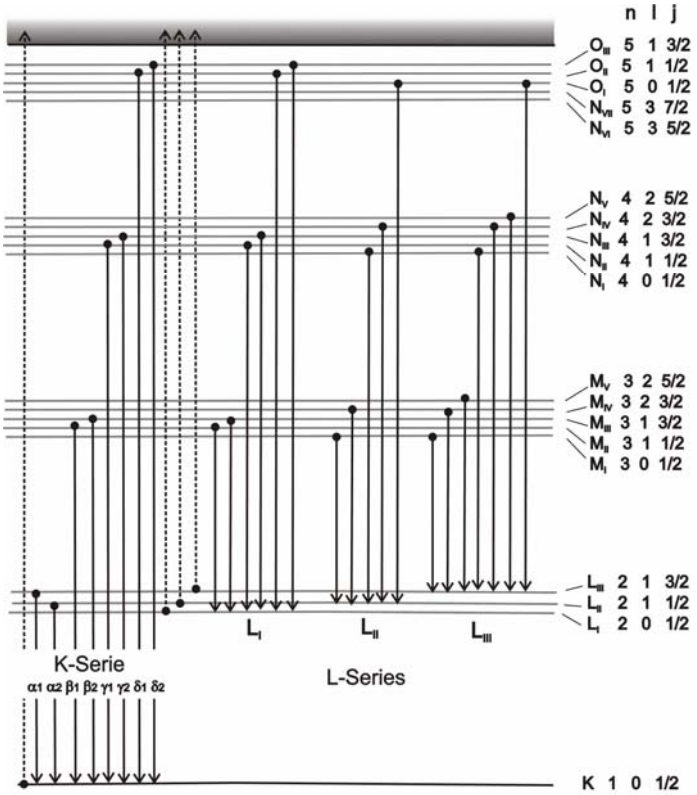

Fig. 4: Level diagram of Pt showing the main K and L transitions. The dotted arrows mark the excitation, the solid arrows the vacancy filling of the electrons. Main quantum number *n*, angular momentum *l*, and total angular momentum *j* are indicated.

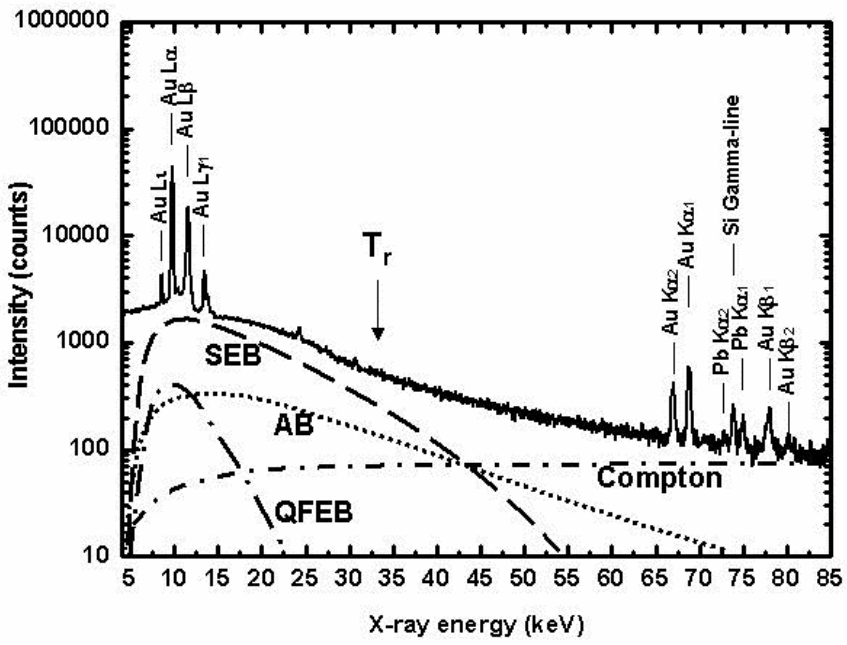

Fig. 5: PIXE spectrum of Au using a 68 MeV proton beam of about 5 nA, measuring time about 45 minutes. All four K lines of Au are clearly visible, also the major L lines. The various background contributions are marked (see text).

Figure 5 shows a X-ray spectrum of a 0.1 μm gold layer on a silicon substrate obtained by 68 MeV protons. The four major K lines are clearly distinguishable, also the four major groups of L lines. The lead K lines are a background contribution of the lead shielding. The silicon γ-line originates from nuclear reactions of the high energy protons with the backing. As the X-rays always appear in groups, single γ-lines cannot be confounded with X-rays. In addition to the peaks, there is a background which consists of:

- Atomic Bremsstrahlung (AB) which is due to the deceleration of bound target electrons in the Coulomb field of the projectile.
- Secondary Electron Bremsstrahlung (SEB) is created by the deceleration of electrons emitted from atoms in the ionization processes. The maximum energy $E_{\max}$ which can be transferred to an electron in a central collision is given by

$$E_{\max} = \frac{4m_e}{M_p} E_p \tag{4}$$

  where m_e and M_p are the mass of electron and projectile, and E_p is the projectile energy. If the collision is not head-on, an energy smaller than E_{max} will be transferred by Coulomb interaction. In the spectrum we observe an intense contribution below E_{max}, decreasing rapidly with increasing energy.
- Quasi Free Electron Bremsstrahlung (QFEB) originates from the quasi free electrons in the solid, and the maximum energy transfer to those electrons is

$$T_r = \frac{m_e}{M_p} E_p \tag{5}$$

  increasing the low energy part of the background. T_r is marked in the spectrum.
- Compton background is due to the Compton scattering of X-rays created in nuclear reactions. Comparing this background for protons and heavy ions at the same velocity, the Compton background is much larger for heavy ions.

Both AB and SEB have an anisotropic behavior and are maximum at 90° with respect to the incoming particle beam. Therefore, for most PIXE set-ups a backward geometry of the detector is preferred.

The ionization cross sections can be calculated theoretically. The most successful theory is the so-called ECPSSR theory. It is based on the Plane Wave Born Approximation (PWBA), where perturbation theory is employed to the transition of an initial state, consisting of a plane wave projectile and a bound atomic electron, to a final state of a plane wave projectile and an emitted continuum electron. Later enhancements include energy loss during the collision (E), the deflection and velocity change of the projectile due to the nuclear Coulomb field (C), the perturbation of the atomic stationary states by the projectile (PSS), and relativistic effects (R). The ECPSSR theory is today widely used and fits very well with measured data above proton energies of 1 MeV and for medium Z. Extensive data tabulations can be found in the compilation of Paul [14] (K shell) and Orlic et al. [15,16] (L shell) and theoretical calculations may be found in [17,18].

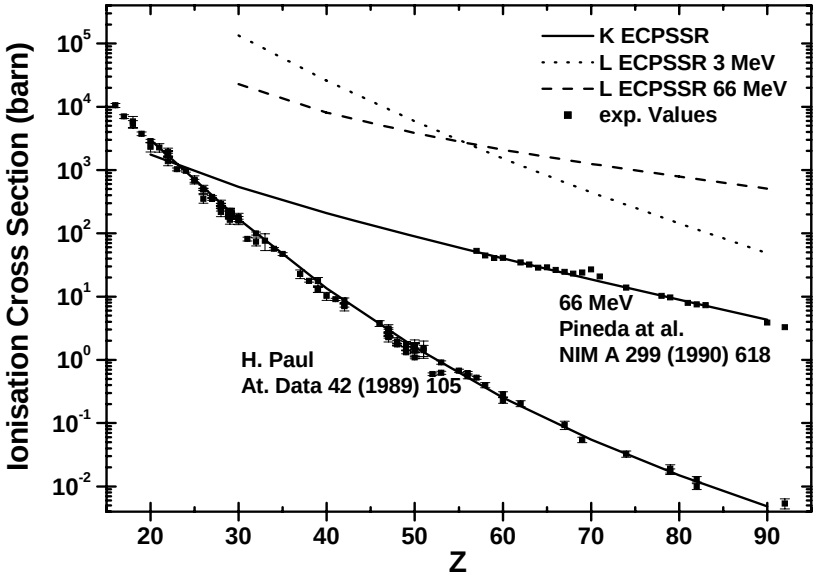

Fig. 6: Cross sections for PIXE. The solid lines represent theoretical ECPSSR calculations for the K lines, the dots the corresponding experimental data. The dotted curve and the dashed curve stands for the L cross sections at 3 MeV and 66 MeV, respectively.

The characteristic X-rays are produced along the flight path of the projectile ion. Therefore, for the production of the X-rays in a given depth, the energy loss of the ion has to be taken into account, as the cross section in a given depth is a function of the energy at that depth.

In addition, for the detection of the X-rays, the attenuation of X-rays in matter has to be considered. In thick samples, the attenuation in the sample will determine the detection limits and the possible analytical depth. The intensity I after a material thickness d of original I_0 intensity of X-rays is given by

$$I = I_0 \exp(-\mu d) \tag{6}$$

with μ being the attenuation coefficient [19]. Table 2 gives some half thickness for various X-ray energies in carbon and copper.

Table 2: Calculated half thickness for X-rays in carbon and copper

X-ray line and energy	$d_{1/2}$ in C (µm)	$d_{1/2}$ in Cu (µm)
Ca Kα, 3.6 keV	78	1.54
Pb Lα, 10.5 keV	2000	4.5
Pb $K\alpha_1$, 75 keV	24 000	800

The maximum analytical depth depends on the target material, influencing the range of the protons as well as the attenuation of the X-rays, and the energy of the X-ray line looked for.

For quantitative analysis, the following equation has to be solved:

$$N_Z = \frac{Y_Z}{N_p \omega_Z b \varepsilon \int_0^{x_{max}} \sigma(x) \exp\left(\frac{-\mu x}{\sin\theta}\right) dx} \tag{7}$$

N_Z is the number of atoms of element Z in the target

Y_Z is the X-ray yield for element Z

N_p is the number of projectiles

ω_Z is the fluorescence yield of element Z

b is the part of the X-rays in the line of interest

ε is the absolute detector efficiency

$\sigma(x)$ is the cross section at a given depth

μ is the attenuation coefficient

θ is the angle of the detector position

x_{max} is the maximum range of the projectiles

In practice, the solving of equation 7 is done using one of the software packages available, like GUPIX [20,21], AXIL, [22,23] or others.

3.2 Experimental set-up

Figure 7 displays the schematic view of a PIXE set-up in vacuum. The beam from the accelerator passes through collimators before impinging the target. For very thin targets the beam intensity can be measured directly with a Faraday cup at the end of the beam line. For thick targets other methods, like a rotating finger in front of the target, have to be applied. Non-conducting targets should either be covered by a very thin film of carbon or sprayed with electron in order to maintain electrical neutrality. This is necessary to prevent electrical discharges, leading to bursts of Bremsstrahlung enhancing the background in the spectra. The sample holder usually allows to mount large number of samples, in order to avoid many openings of the chamber with the necessary pumping times.

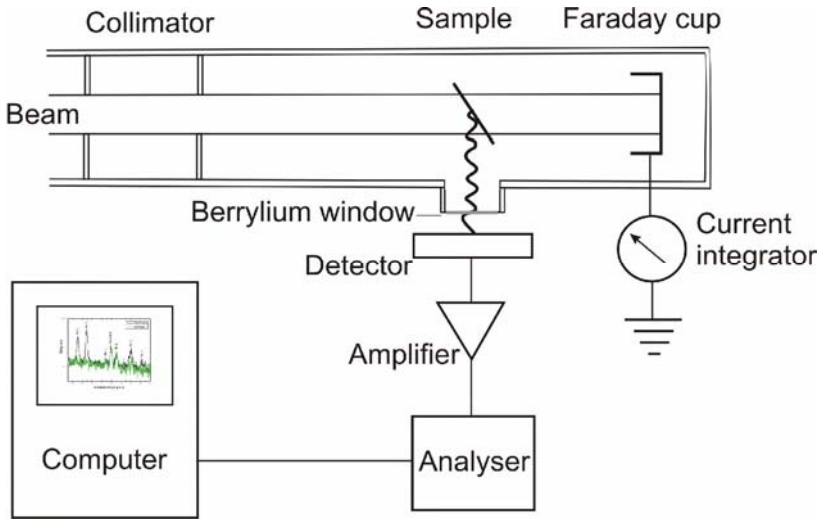

Fig. 7: Schematic view of a PIXE set-up in vacuum

One of the advantages of PIXE when using protons as projectiles, is the easy extraction of the proton beam from the vacuum of the beam line to ambient atmosphere through thin foils. This allows the analysis of samples which cannot be brought into vacuum. However, the analysis of very light elements (Na to P) becomes difficult if not impossible, due to the absorption of the low energy X-ray

lines in the air path between target and detector. Also the determination of the beam intensity cannot be done directly. Figure 8 shows the photograph of the set-up at the Ionenstrahllabor of the Hahn-Meitner-Institut Berlin. The beam intensity is in that case measured via an ionization chamber. To maintain the geometry of the set-up, two laser cross-hairs mark the beam spot on the sample.

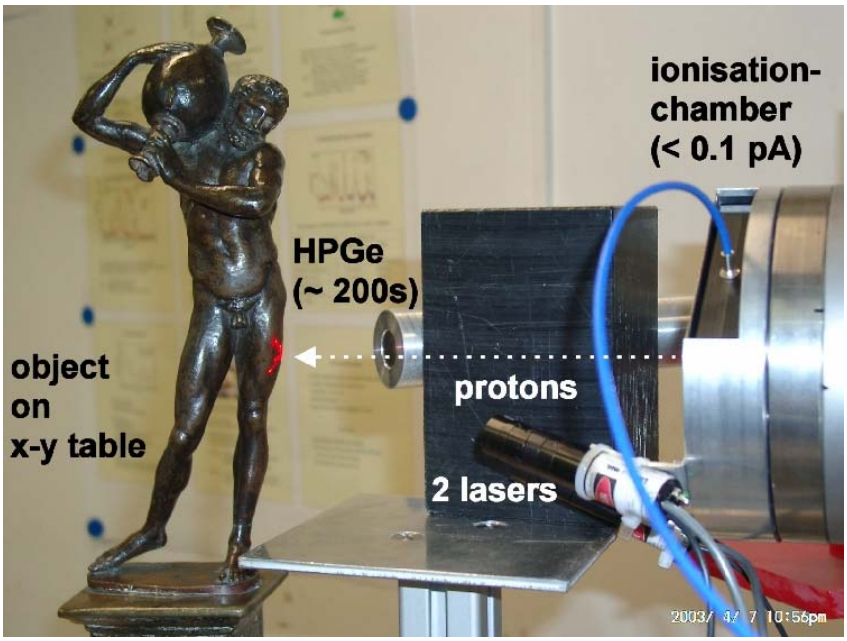

Fig. 8: The PIXE set-up at the Ionenstrahllabor of the Hahn-Meitner-Institut. The 68 MeV proton beam from the cyclotron exits the vacuum of the beam line via a thin Kapton foil.

As detectors, either Si(Li) detectors or high purity germanium detectors (HPGe) may be used. Si(Li) detectors offer the advantage of better resolutions at low X-ray energies, typically 160 eV at 5.9 keV. The disadvantage of the Si(Li) is the low detector efficiency above 25 keV. HPGe detectors provide good efficiency even for the K X-ray energies of the very heavy elements, however, their energy resolution is usually only about 180 eV at 5.9 keV.

The signals of the detector are amplified, given to an analog/digital converter and then processed by a multi channel analyzer, usually combined with a computer to allow on-line display of the spectra. The identification of the elements present in the sample can be done during the measurements, whereas the final de-convolution of peak heights to concentrations is done off-line.

3.3 Examples

The risk of beam damage to the samples is generally very low, when keeping the beam intensity low and having the objects in normal atmosphere. Therefore, PIXE is considered to be nondestructive. Hence, a lot of applications of PIXE involve the measurements on unique and precious objects from art and archaeometry.

3.3.1 Chinese bowl: ancient or relatively modern?

Figure 9 shows a 38 cm large Chinese bowl, weighing 4.8 kg. The two art historical expert opinions for this bowl are contradictory: A Japanese report dates the bowl back to the Ming dynasty, according to a stamp on the bottom indicating that the bowl was produced between 1522–1566. The other report states that shape and decoration are modern copies of the Ming dynasty, yet the utmost age of the bowl is about 100 years. The age of the bowl is of fundamental importance for its value, therefore, methods were needed to determine the manufacturing time. As thermo-luminescence cannot be

applied on porcelain, only indirect dating is possible. One possibility is the identification of the characteristic elements in the pigments because recipes vary over time [24–26]. Before the middle of the 19th century, green colors were copper based, later chromium containing pigments appeared.

Fig. 9: Chinese bowl after the analysis

The solid line in the left side of Fig. 10 shows the spectra of the green ornament: A clear copper signal is visible in the spectrum, together with lead. The lead comes from lead oxide which is used in porcelain colors to reduce the necessary firing temperatures. No chromium is visible in the spectrum on the green ornament. For comparison, a modern porcelain, being decorated with green color in the same color saturation was measured (dashed line). Here, no copper, but a large chromium signal is visible, together with some cadmium. Chromium in green porcelain signifies a modern one, but on the reverse modern recipes list copper as pigment as well.

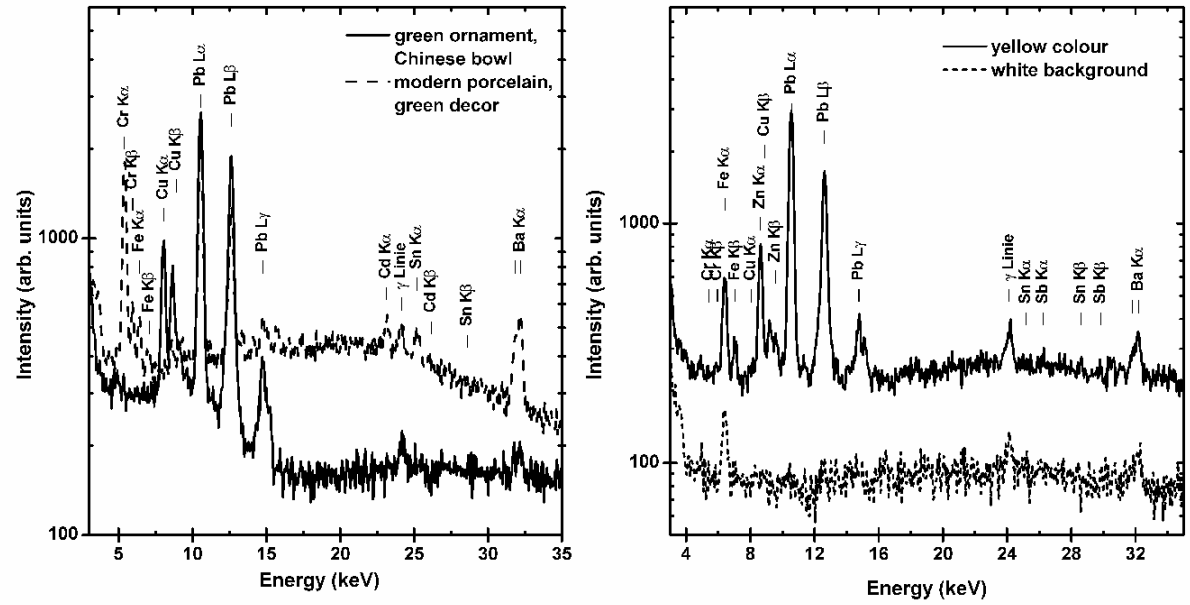

Fig. 10: High-energy PIXE spectrum of the Chinese bowl. Left: the spectrum of the green color, showing no Cr signal compared with the spectrum of a modern porcelain. Right: The spectrum of the yellow color in comparison with the spectrum of the white background of the bowl.

Hence, also the yellow color was measured. The right side of Fig. 10 displays the results from the yellow part compared to the white porcelain itself. In the yellow color zinc and lead are found, but no antimony is visible in the spectrum. In all recipes up to about 1850, zinc is combined with iron and antimony: the amount of antimony in Sb_2O_3 being about twice the amount of zinc in ZnO. Only recently, solely ZnO was used together with iron as a yellow pigment. Hence, the absence of antimony in the spectrum confirms the report stating a maximum age of the bowl of about 100 years.

3.3.2 Prussian medals

In the frame of a thesis describing "gap-filling on enamel illustrated by three medals of the German Historic Museum" [27] these medals were analyzed by high-energy PIXE. The main issue of the thesis was to find a suitable material for the completion of the medals in the restoration process. Mock-ups were prepared to examine the adhesive properties of selected conservation materials on gold and enamel. To specify the composition of the mock-ups, the metal composition of the medals was analyzed using high-energy PIXE. The aim of the PIXE analysis was the determination of the elemental composition and, especially, the distinction between massive and gilded parts. The advantage of high-energy PIXE is, that the K X-rays of the heavy elements are excited. Therefore, the intensity ratio of the K/L lines provides additional information about depth besides the mere elemental composition.

Figure 11 shows the spectrum of medal 21.338a compared to the results of a thin gold foil measured in the same set-up. The intensity ratio of the gold $L\alpha/K\alpha_1$ line of the medal in this spectrum is 1.25, whereas the thin gold foil yields a ratio of 44. For comparison, a 1 cm thick lead sample gives a ratio of $L\alpha/K\alpha_1$ of 1.3. Hence a thin gold layer, i.e. gilding, on top of a different material can be excluded. Similar rations were observed on all investigated spots, meaning that the support for the enamel was made of a massive gold alloy. The composition of the medal was determined to be 75% gold, 15% silver and 10% copper (in weight %).

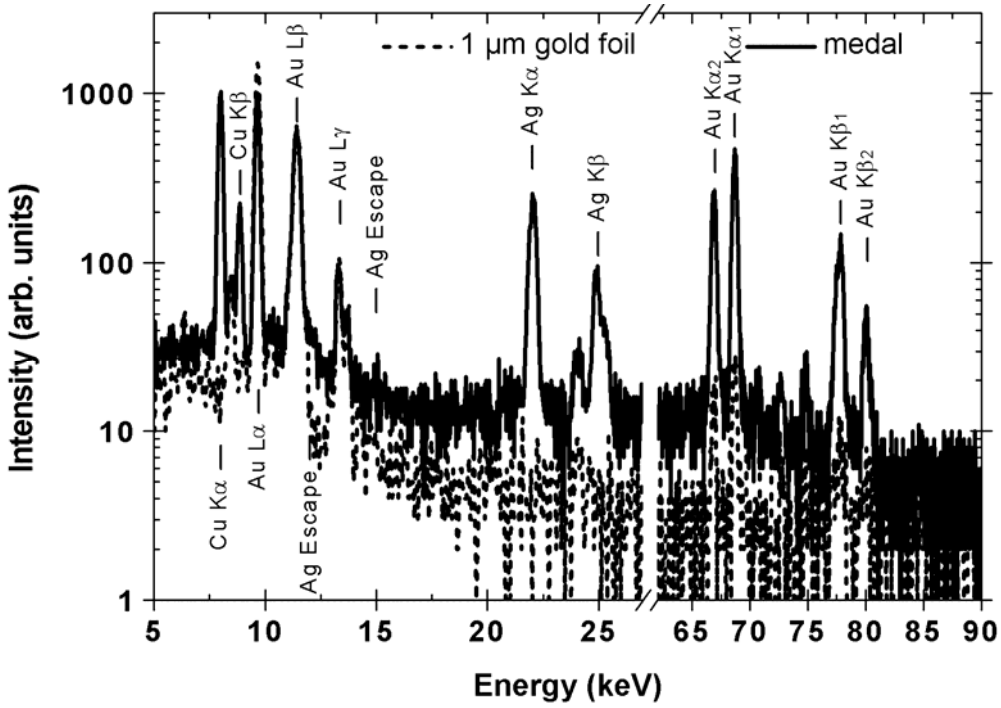

Fig. 11: Spectra of the Prussian medal (solid) and a thin gold foil (dashed). The large intensity of the gold K lines implies the use of a massive gold alloy, a gilding can be excluded.

4 Rutherford back-scattering, elastic recoil detection analysis

4.1 RBS (Rutherford Back-Scattering) spectroscopy

For the RBS method a sample is irradiated with light energetic ions, typically hydrogen, helium, nitrogen or neon of a few MeV. At a backward angle, close to 180° relative to the beam direction, the number and the energy of projectile ions backscattered from the target are measured. Since these values are dependent on the mass respectively on the nuclear charge of the scattering atoms and because the projectiles sustain an energy loss in the material it is possible to determine the elemental composition as a function of depth. The mass identification of the target atoms results from the energy of the backscattered projectile, typically measured by means of a surface-barrier detector.

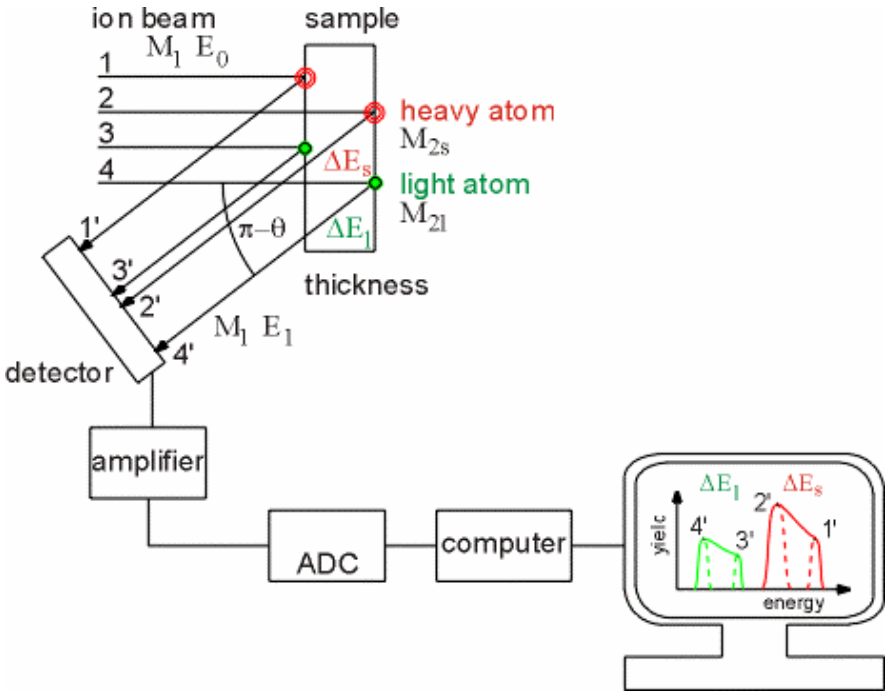

Fig. 12: Schematic view of a RBS set-up

Using heavier ions e.g. ^{14}N allows a better mass separation compared to so called standard RBS using H- or He-ions as projectiles. The thickness of the layer respectively the elemental concentration as a function of depth is determined from the energy difference of the backscattered projectile referring to the corresponding maximum energy for the scattering at a surface atom, given by the kinematical factor:

$$E_1 = k_p E_o \tag{8}$$

with

$$k_p = \left(\frac{M_p / M_r \cos\theta + \sqrt{1 - (M_p / M_r)^2 \sin^2\theta}}{1 + M_p / M_r} \right)^2 \tag{9}$$

In the case of thicker samples the mass identification may be complicated due to the superposition of the spectra originating from the various sample components. The number N_p of the measured backscattered projectile ions gives the concentration of the corresponding element:

$$N_r = \frac{N_p}{\sigma_p \Delta\Omega N_0} \tag{10}$$

with $\Delta\Omega$ the known solid angle for the setup and N_0 the number of the incident projectile ions.

For the energies used, the differential Rutherford cross section for the scattering of a projectile with the nuclear charge Z_p from a target atom with the elemental number Z_r can be calculated exactly:

$$\frac{d\sigma_p}{d\Omega} = \left(\frac{Z_r Z_p e^2}{2E_0}\right) \frac{1}{\sin^4\theta} \frac{\left(\cos\theta + \sqrt{1-\left(M_p/M_r \sin\theta\right)^2}\right)^2}{\sqrt{1-\left(M_p/M_r \sin\theta\right)^2}} \tag{11}$$

Therefore, no free parameter is left, i.e., RBS is a standard free, absolute method. Since the scattering probability increases with Z_r^2 RBS is more sensitive for heavier components of the sample. The scattering to large angles from atoms with masses close to or even below the projectile mass is not possible, therefore, these light elements are not detectable. Possible errors in the used stopping power result in errors of the calculated depth distributions. Close to the surface, a depth resolution of 10 nm can be achieved. The typical analytical depth is about 2 µm.

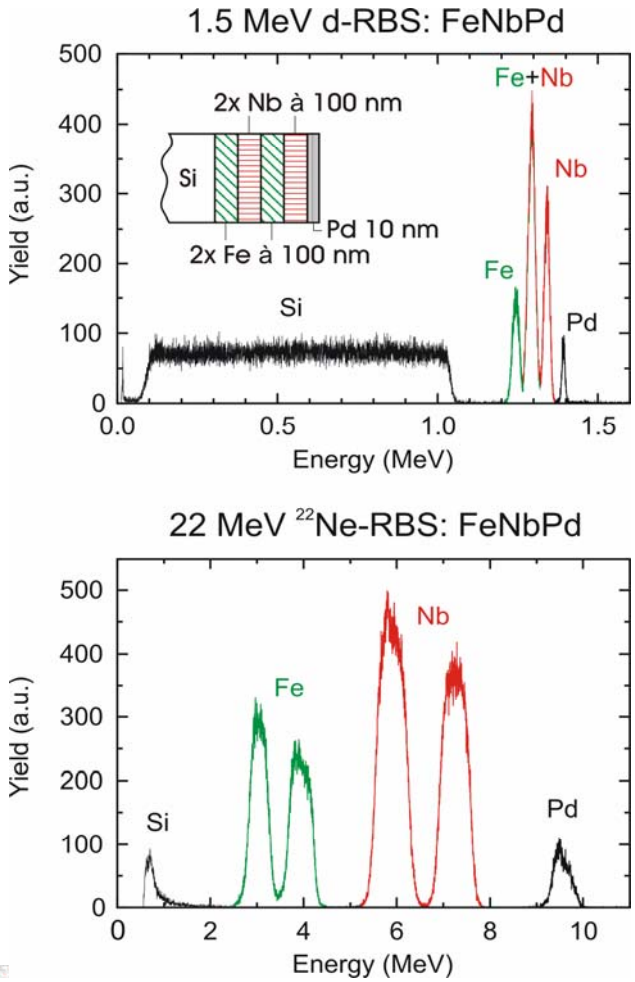

Fig. 13: Comparison of standard RBS (here with deuterons) and heavy ion RBS applied to the same sample. The clear separation of the elements of the FeNbPd-multilayer structure (lower picture) results from the much better mass resolution of the heavy ion RBS.

4.2 ERDA – Elastic Recoil Detection Analysis

ERDA is based on the same principles as RBS. Instead of measuring the backscattered projectiles, the recoiled atoms from the sample are measured (see Fig. 14). The mass identification can be done by measuring the energy and, e.g., the time-of-flight of the recoiled atoms. According to

$$E = \frac{M}{2} v^2 \tag{12}$$

it is possible to identify and separate the various masses in the two-dimensional scatterplot time vs. energy [28]. Again, the cross sections and therefore the number of atoms in the target can be calculated directly using the Rutherford cross sections. Using very heavy ions, no restrictions in elements to be detected exist. All elements from hydrogen up to the very heavy ones can be measured with comparable sensitivities, the sensitivity for hydrogen is even enhanced by a factor of four, according to equation 13, where the formula for the Rutherford cross sections was transformed to the system of the recoiled atoms:

$$\frac{d\sigma_r}{d\Omega} = \left(\frac{Z_p Z_r e^2}{2E_0} \right)^2 \left(\frac{M_p + M_r}{M_r} \right)^2 \frac{1}{\cos^3 \phi} \tag{13}$$

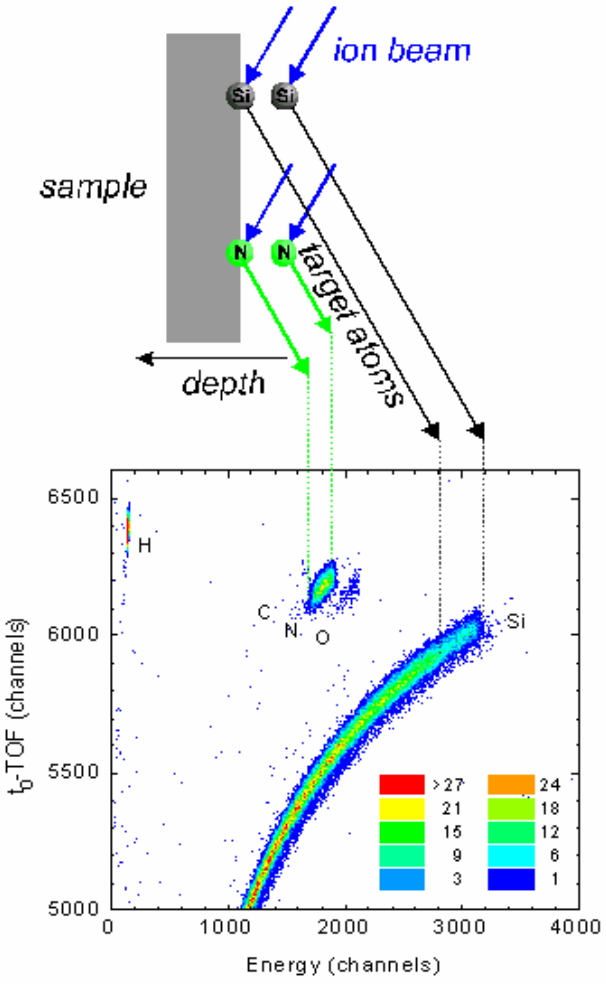

Fig. 14: Schematic view of a ERDA principle together with a scatterplot time-of-flight versus energy of a SiN_x:H layer on Si scattered to 60° relative to the direction of the irradiating beam of 230 MeV ^{129}Xe-ions

Similar to RBS, depth profiles may be derived from the spectra. Close to the surface, a depth resolution of 10 nm can be achieved. The typical analytical depth is about 2 µm.

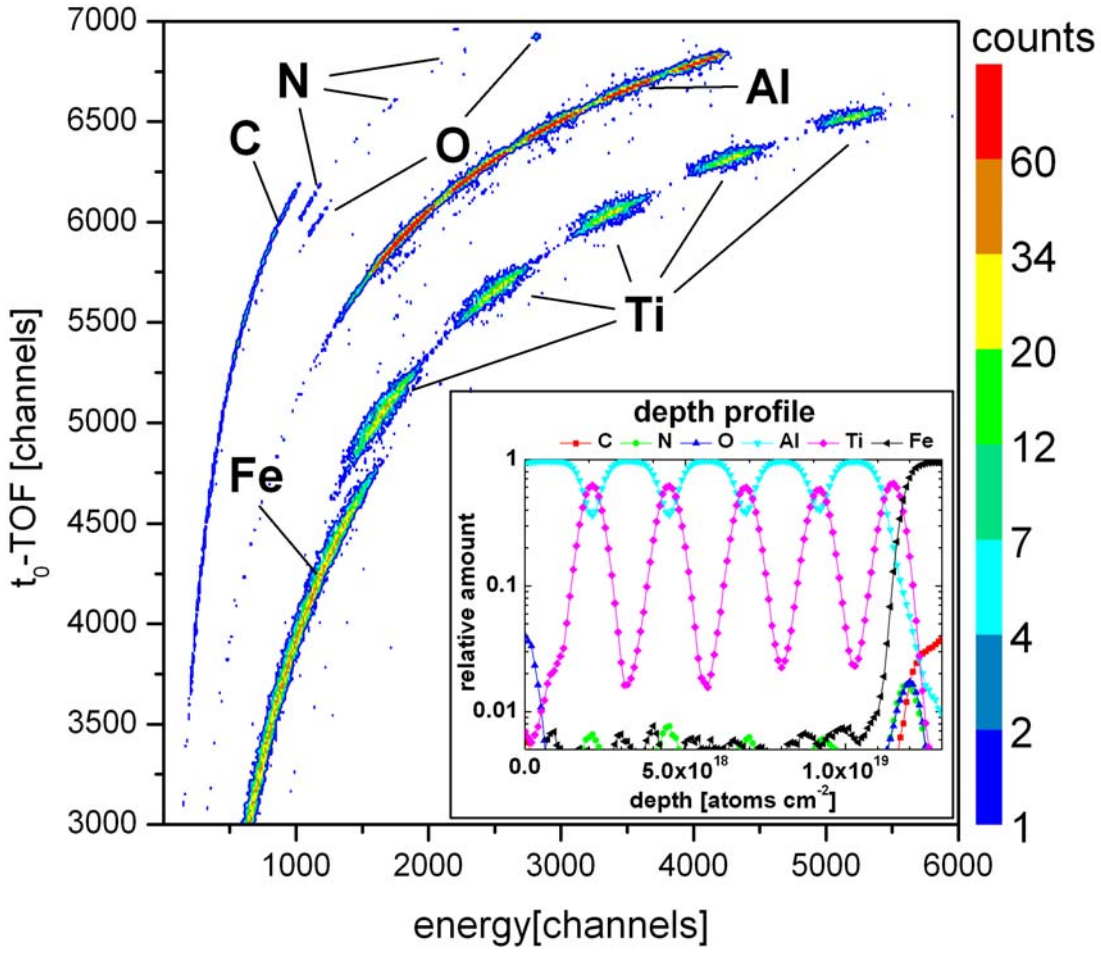

Fig. 15: ERDA-measurement of a certified reference material (5 double layers of Al/Ti on steel). In the scatterplot of the time of flight (TOF) vs. energy, the different elements can be well separated and their energy spectra are extracted from the data. Using stopping power data, the energy spectra can be converted into depth profiles (inlet). The five double layers can be easily distinguished, as well as O and N contaminations on the surface and the multilayer/steel interface.

5 Conclusions

The whole field of ion beam analytical techniques cannot be presented in a single paper. The presented methods, PIXE, RBS, and ERDA, have all their specific advantages and drawbacks. PIXE is a very fast method when applied to thin samples, allowing determinations of trace elements on huge amounts of samples. As PIXE can be applied in a non-destructive way, measurements on very unique and precious objects are possible. RBS and ERDA provide the quantitative elemental composition as a function of depth up to a few µm. The elemental sensitivity for heavy elements in light matrices is better for RBS, however, light elements can be detected by ERDA. The success of the analysis depends on the appropriate choice of the analytical technique.

References

[1] J. Rabalais, Principles and Applications of Ion Scattering Spectrometry: Surface Chemical and Structural Analysis, Wiley (2002).

[2] J.R. Tesmer, M. Nastasi, Handbook of Modern Ion Beam Materials Analysis, MRS (1995).

[3] M.A. Respaldiza, J. Gómez-Camacho, Applications of Ion beam analysis techniques to arts and archaeometry, Universidad de Sevilla, (1997).

[4] J.F. Ziegler, J.P. Biersack, U. Littmark, The Stopping and Ranges of Ions in Matter 1, 1985 (Plenum, New York).

[5] H. Paul, D. Semrad, A. Seilinger, Nucl. Instr. Methods in Phys. Res. B61 (1991) 261.

[6] http://www.srim.org

[7] J. Chadwick, Phil. Mag. 24 (1912) 54.

[8] T.B. Johansson, K.R. Akelsson, S.A.E. Johansson, Nucl. Instr. Meth. 84 (1970) 141.

[9] P. Hovington, D. Drouin, R. Gauvin, Scanning 19 (1997) 1.

[10] http://www.gel.usherb.ca/casino/index.html

[11] W. Bambynek, B. Crasemann, R.W. Fink, H.U. Freund, H. Mark, C.D. Swift, R.E. Price, P. Venugopalo Rao, Rev. Mod. Phys 44 (1972) 716.

[12] W.Bambynek, Proceedings of International Conference on Inner Shell Ionization X84 (1984) Leipzig.

[13] J. H. Scofield, Exchange correction of K X-ray emission rates, Phys Rev A9 (1974) 1041.

[14] H. Paul, J. Sacher, At. Data and Nucl. Data Tables 42 (1989) 106.

[15] I. Orlic, C.H. Sowe, S.M. Tang, At. Data and Nucl. Data Tables 56 (1994) 160.

[16] R.S. Sokhi, D. Crumpton, At. Data and Nucl. Data Tables 30 (1984) 50.

[17] M. H. Chen, B. Crasemann, At. Data and Nucl. Data Tables 33 (1985) 217.

[18] O. Benka, A. Kropf, At. Data and Nucl. Data Tables 22 (1978) 219.

[19] H. Hubbell, S.M. Seltzer, Tables of X-Ray Mass Attenuation Coefficients and Mass Energy-Absorption Coefficients, Originally published as NISTIR 5632, National Institute of Standards and Technology, Gaithersburg, MD 1995

[20] J.A. Maxwell, W.J. Teesdale, J.L. Campbell, Nucl. Instr. and Meth. B95 (1995) 407.

[21] http://www.physics.uoguelph.ca/PIXE/index.html

[22] P. Van Espen, K. Janssens, I. Swenters, AXIL X-Ray Analysis software. Canberra Packard, Benelux (1989) 48.

[23] http://www.iaea.org/OurWork/ST/NA/NAAL/pci/ins/xrf/pciXRFdown.php

[24] E. Speel, H. Bronk, Berliner Beiträge zur Archäometrie 18 (2001) 43.

[25] W.D. Kingery, P.B. Vandiver, 2nd Proceedings of a Society Meeting on Ceramic history and archaeology, 87th annual meeting of the American Ceramic Society, (1985).

[26] U. Müller, M. Tirge, D. Kruschke, K. Adam, BAM Forschungsbericht 217, Berlin.

[27] K. Ebert, thesis at the Fachhochschule für Wirtschaft und Technik Berlin (1997).

[28] W. Bohne, J. Röhrich, G. Röschert, Nucl. Instr. and Meth. B136-138 (1998) 633.